

Machine learning of XY model on a spherical Fibonacci lattice

Chen-Hui Song,^{1,2,3} Qu-Cheng Gao,¹ Xu-Yang Hou,¹ Xin Wang,¹ Zheng Zhou,¹ Yan He,⁴ and Hao Guo^{1,*}

¹*Department of Physics, Southeast University, Jiulonghu Campus, Nanjing 211189, China*

²*Chien-Shiung Wu College, Southeast University, Jiulonghu Campus, Nanjing 211189, China*

³*Tsinghua Shenzhen International Graduate School, Tsinghua University, Shenzhen 518055, China*

⁴*School of physics, Sichuan University, Chengdu, Sichuan 610064, China*

We study the XY model on a spherical surface by using Monte Carlo simulations and machine learning methods. Instead of a traditional latitude-longitude lattice, we consider a much more homogeneous spherical lattice, the Fibonacci lattice. After obtaining the equilibrium spin configurations by classical Monte Carlo annealing, we propose a graph-convolutional-network based method to recognize different phases, and successfully predict the phase transition temperature. We also apply the density-based spatial clustering of applications with noise, a powerful machine learning algorithm, to unravel the merging path of two vortices with different topological charges on the sphere. Our results provide reliable predictions for future space-based experiments on ultracold atomic gases confined on spherical lattice in the microgravity environment.

I. INTRODUCTION

The XY model[1], although very simple, is of great importance to a lot of quantum many-body systems, such as the liquid helium, antiferromagnetic insulators, and superconductors[2]. In the two-dimensional (2D) situation, the XY model has inspired the research boom on topological phase transitions[3–5]. During the last half century, there have been tons of studies on various aspects of XY model[6–19]. Experimentally, the XY model can be emulated by ultracold atoms confined in optical lattices[20]. In recent years, the quickly developing space-based technique has stimulated new experimental proposals to confine ultracold boson gases on a spherical surface in microgravity environments[21–26]. Due to the close relation between Bose-Einstein condensate (BEC) and XY model, it is natural to consider the XY model trapped on a spherical lattice. However, there does not exist a completely isotropic lattice on a spherical surface like the 2D square lattice, which prevents a direct analytical study on such a model. Therefore, suitable numerical methods must be developed to make reliable and instructive predictions. Fortunately, this can be achieved by the aid of powerful tools in processing big data, such as the machine learning. During the last several years, these methods in computer science have been successfully introduced to the physics community, and achieved tremendous and unexpected progresses[27–39].

In this paper, we focus on the spherical XY model. We first consider an approximately uniform lattice, the Fibonacci lattice, on the surface of a sphere, which has a much better isotropy than the traditional latitude-longitude lattice. Then, with the help of Monte Carlo simulation, we find the corresponding spin configurations. Multiple vortices onset at low temperatures and the total topological charge is always 2 due to the topology of 2D sphere. By using the graph-convolutional-network (GCN) model, we successfully predict the Berezinskii-Kosterlitz-Thouless (BKT) phase transition temperature. Finally, we apply the density-based spatial clustering of applications with noise (DBSCAN) to give the dynamical trajectory of these vortices, which shows the merging of different vortices during the MC annealing. Our results provide a solid theoretical reference for future space-based experiments on spherically confined ultracold atomic gases.

II. THE SPHERICAL XY MODEL

A. The XY Model

The 2D classical XY model on a square lattice is described by the Hamiltonian

$$H = -J \sum_{\langle i,j \rangle} \mathbf{s}_i \cdot \mathbf{s}_j = -J \sum_{\langle i,j \rangle} \cos(\theta_i - \theta_j) \quad (1)$$

*Electronic address: guohao.ph@seu.edu.cn

where J is the interaction constant, \mathbf{s}_i the spin with angle θ_i at site i , and the sum is taken over all pairs of nearest-neighbor spins. At zero temperature, the system stays at the ground state in which all spins are aligned in the same direction. There are also excitations with nontrivial topology, such as vortices and anti-vortices, which onset below the BKT transition temperature T_c . An interesting question is: What happens when all spins are confined on a spherical surface S^2 ?

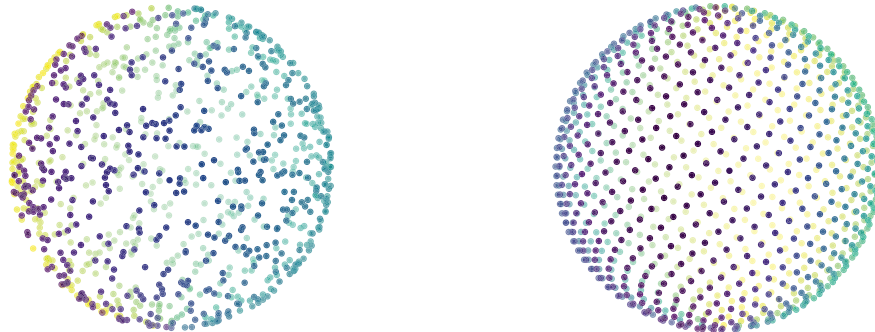


Figure 1: (Left panel) Random lattice on a spherical surface. (Right panel) Fibonacci lattice on a spherical surface.

B. The Fibonacci Lattice

Note the map of a XY model onto a sphere is nontrivial since the 2D plane is topologically different from a spherical surface. On a square lattice, the ordinary XY model described by Eq.(1) is isotropic and the lattice site is evenly distributed. When confined on a spherical surface, some important issues must be carefully treated. For example, how can we arrange the spins as homogeneous as possible? How is the Hamiltonian revised with respect to a certain spherical lattice? Obviously, the expression on the far right-hand-side of Eq.(1) does not apply any more. A regular and convenient choice of coordinate lattice seems to be the latitude-longitude lattice. However, it is highly inhomogeneous: The site density near the north or south pole is much denser than anywhere else. If a spherical lattice is totally isotropic, each site of it must belong to the vertices of a regular polyhedron. There are only five different types of regular polyhedrons, among which the regular dodecahedron has the largest number of vertices: 20. In other words, a totally isotropic spherical lattice has at most 20 sites, which is too small to a XY model. In an optimal point sampling, the area represented by each site must be almost the same. For a spherical lattice with a large number of sites, an approximately uniform distribution can be realized by the Fibonacci lattice[40, 41], in which the i -th site on a unit sphere is defined by

$$x_i = \sqrt{1 - z_i^2} \cos(2\pi\phi), y_i = \sqrt{1 - z_i^2} \sin(2\pi\phi), z_i = \frac{2i - 1}{N} - 1, \quad (2)$$

for $i = 1, 2, \dots, N$. Here N is the total number of sites, and $\phi = \frac{\sqrt{5}-1}{2}$ is the golden ratio. When N is large, the $i = 1, N$ sites approach the southern and northern poles of the sphere respectively. Figure.1 shows the comparison between a random and a Fibonacci lattices on a sphere. Apparently, the site distribution of the latter is much more uniform.

Since the spherical Fibonacci lattice is not strictly isotropic, we introduce a cutoff distance r_c such that the interaction is allowed only when the separation between each pair of spins is less than r_c . Moreover, the distance between an arbitrary site and its nearest neighbour is not a constant, and we accordingly assume a Gaussian type interaction

$$H = -J \sum_{\langle i,j \rangle} e^{-\alpha r_{ij}^2} \mathbf{s}_i \cdot \mathbf{s}_j \quad (3)$$

where the constant α determines the scale of the short-range interaction, and r_{ij} is the distance between the sites i and j . Each spin is normalized to be unit-lengthed, and is locally confined on the tangent plane at its site.

To verify the uniformity of Fibonacci lattice, we choose a sphere of radius $R = 10$, and sprinkle a Fibonacci lattice with $N = 1000$ sites on its surface. For each site, the lattice points that fall in its domain of radius r_c are referred to

its neighbours. If $r_c = 1.1395$, we find that 850 sites have 4 neighbours, 76 sites have 3 neighbours, and 74 sites have 5 neighbours. Basically, this is almost the best approximation to a 2D square lattice for spherical lattices. Note there are $850 \times 4 + 76 \times 3 + 74 \times 5 = 3998$ neighbours. Equivalently, interactions are allowed between 3998 pairs of spins. The distribution of pair separations are outlined in Table.I.

Number of pairs	Average distance	Standard deviation	Median	Minimum	Maximum
3998	1.1455	0.0816	1.1194	0.9777	1.2977

Table I: Distribution of pair separations.

C. Effect of the topology of S^2

Before discussing the XY model on a spherical surface, we briefly overview some key points of the 2D square-lattice XY model. At zero temperature, the ground state is a topologically trivial state with $\theta_i = \text{constant}$. At temperatures above zero, topological defects called ‘‘vortices’’ appear in the form of bound vortex-antivortex pairs. As the temperature increases, the vortex-antivortex pairs start to unbind at the BKT temperature T_c . To compare with the spherical-lattice XY model, we also include the Gaussian-type interaction to the square-lattice XY model, and introduce r_c to control the range of interaction. Then, we use the Monte Carlo (MC) simulation to study the XY model on a 30×30 lattice of unity lattice constant, and the results are visualized in Fig.2. In the left panel, we set $r_c = 1.0$ and the model reduces to an ordinary XY model. It can be seen that many vortices appear in bound pairs. In the middle and right panels, $r_c = 2.0$ and 3.0 respectively. We find that the number of vortices decreases significantly. This is understandable since r_c indicates the scale of local orderedness. As it increases, the pair size must increase. Thus the visible vortex pairs per area reduce correspondingly. This is clearly confirmed by Fig.2.

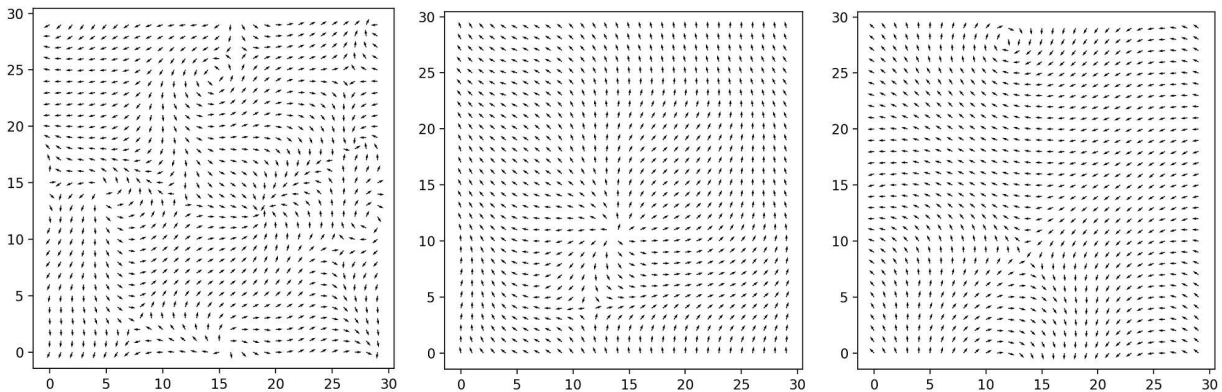


Figure 2: Monte Carlo study of a 2D square-lattice XY model. (Left panel) $r_c = 1.0$. (Middle panel) $r_c = 2.0$. (Right panel) $r_c = 3.0$. The temperature is $T = 0.0001K$. Obviously, the vortex density decreases as the interaction range increases.

When mapped onto a spherical surface, since all spins are confined on the tangent plane at each site, the spins actually belong to a tangent vector field X on S^2 , which is nondegenerate. The Poincaré-Hopf theorem[42] states that

$$\sum_i \text{ind}_{x_i}(X) = \chi(S^2). \quad (4)$$

Here $x_i \in S^2$ denotes the zeros of the vector field X , $\text{ind}_{x_i}(X)$ means the index of X at x_i , and $\chi(S^2)$ is the Euler characteristic of S^2 , which is 2. The zero x_i in fact corresponds to a vortex, since the center of a vortex is a zero point of a vector field. Moreover the index at x_i equals to the product of its sign and multiplicity, where the sign corresponds to the topological charge, and the multiplicity is usually 1. Physically, the Poincaré-Hopf theorem states that the net topological charge of a spherical-lattice XY model is always 2. This result is independent of temperatures, hence vortices must onset even at zero temperature, which is essentially different from the square-lattice XY model.

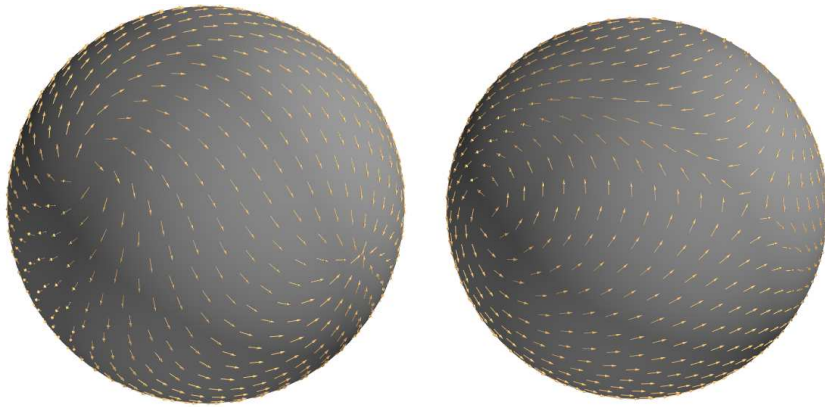


Figure 3: Monte Carlo study of a spherical Fibonacci-lattice XY model after a partial annealing, in which the chosen parameters are $R = 10$, $N = 1000$, $T = 0.001K$ and $r_c = 1.1395$. (Left panel) Front side. (Right panel) Back side. Here the “front” and “back” sides are simply convenient references.

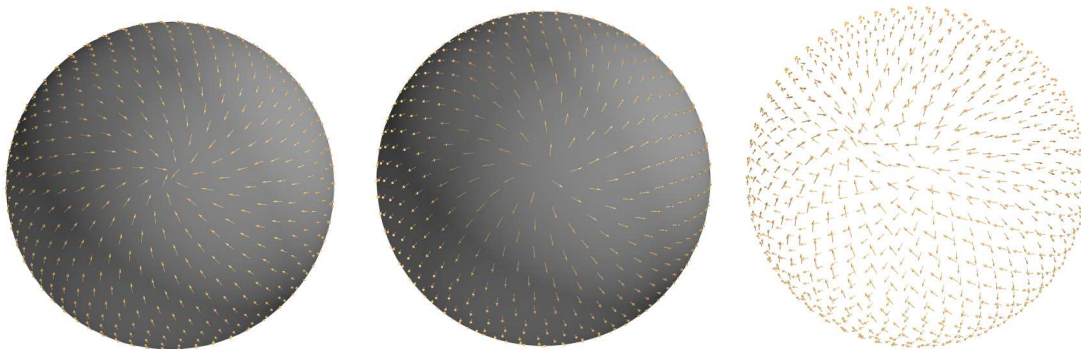


Figure 4: Monte Carlo study of a spherical Fibonacci-lattice XY model after a complete annealing. (Left panel) A vortex on one side. (Middle panel) Another vortex on the opposite side. (Right panel) Perspective drawing.

III. SPIN CONFIGURATIONS

To start a numerical simulation, we choose $R = 10$, $N = 1000$, $T = 0.001K$ and $r_c = 1.1395$. Initially, the spins are randomly oriented, and evolve under the MC annealing afterwards. The simulation runs 1.5×10^8 steps until the spin configuration is stable. It can be found that multiple vortices appear during the annealing. Figure.3 presents an intermediate result when the annealing runs 10^5 steps, and there are at least four vortices (For more details, please refer to the cartoons in supplementary materials). As the simulation continues, some vortices disappear or merge with one another. We show the stable spin configuration in Fig.4 after running 1.5×10^8 steps, and find that only two unpaired vortices survive. Moreover, these two vortices tend to move away from each other during the annealing and finally reside at two nearly opposite sites on the sphere. Note they are not necessarily located at the two poles of the Fibonacci lattice but any two (approximately) opposite sites. The topological charges of the two vortices are obtained by

$$n = \frac{1}{2\pi} \oint \nabla\theta \cdot d\mathbf{l} \quad (5)$$

where the integral is evaluated along a closed curve encircling the centre of vortices. Using this formula, it can be found that both vortices have the charge $+1$, which agrees with our previous analysis based on Poincaré-Hopf theorem. This also explains why the vortices move as far as possible from each other: It is because the repulsion between them. In this situation, our result about the XY model on a spherical Fibonacci lattice also agrees with that on a spherical random lattice[43]. However, this is not the only stable spin configuration in the end. It actually depends on our choice of parameters. In Figure.5, we present the final stable spin configuration by choosing $R = 10$, $N = 3000$, $T = 0.001K$ and $r_c = 0.9$, after the annealing runs 1.5×10^8 steps. There are eight vortices, five of which have charge $+1$, three have charge -1 . Thus, the total topological charge is also $+2$, just as expected. This is quite reasonable. In

fact, the lattice in this case becomes much larger than the $N = 1000$ case with respect to a typical pair of adjacent sites. Thus, the distance between vortices is effectively larger and the interaction becomes relatively smaller, which may prevent the merging of vortices when the annealing goes on. This phenomenon is not found in the random-lattice case[43].

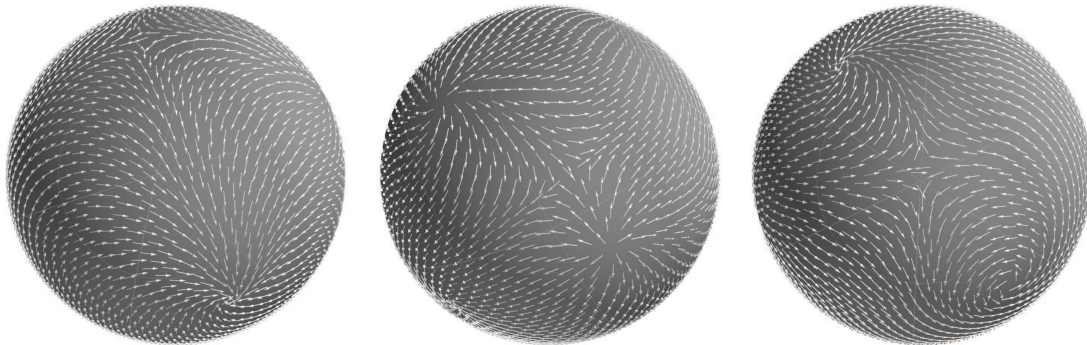


Figure 5: Monte Carlo study of a spherical Fibonacci-lattice XY model after a complete annealing, in which the chosen parameters are $R = 10$, $N = 3000$, $T = 0.001K$ and $r_c = 0.9$. The spin configuration is presented from three different directions to show all 8 vortices.

IV. PHASE TRANSITION TEMPERATURE

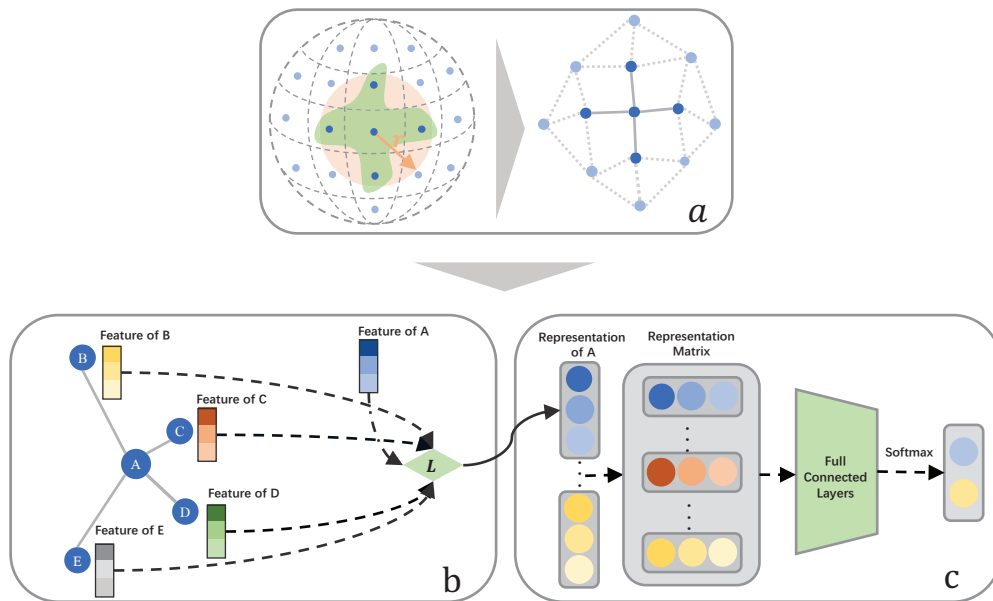


Figure 6: Flow charts for phase classification of spherical XY model based on GCN. Panel a shows how to extract a graph structure from a spherical Fibonacci lattice. Panel b indicates that the input features are aggregated by the Laplacian matrix. Panel c shows that the classification confidences are finally obtained by using the fully connected layer.

To determine the phase transition temperature, a powerful tool is the newly developed paradigm, the machine learning method. There have been plenty of successful examples, among which the neural network has particular advantages due to its strong generalization ability. Even the simplest three-layer fully connected neural network (FCN) can well recognize different phases of Ising model[29]. However, for topological phase transitions of square-lattice XY models, FCN does not work equally well since it can not effectively capture the local spatial information, which may be directly related to the local orderedness. An alternative tool is the convolutional neural network (CNN), which has proved its powerfulness in many situations[44, 45]. CNN relies on the convolutional kernels to extract local

features from an input object, which usually requires the information distribution has a spatial translation invariance. Obviously, this is not satisfied by a spherical lattice. Even the Fibonacci lattice is just approximately uniform. Here we propose a new method for phase recognition based on the graph convolutional network (GCN)[46, 47], which can be easily apply to the spherical lattice and even irregular lattices.

GCN is a generalization to the traditional CNN based on the graph data structure. It can effectively aggregate the local spatial information, and thus realize the classification of vertices and graphs. Details of GCN can be found in Appendix.A, and Figure.6 shows the flow charts to classify different phases of the spherical XY model by GCN. Here we give a very simple introduction of the procedure. For a $N = 1000$ spherical Fibonacci lattice, we set $r_c = 1.1395$ such that most sites have 4 neighbors. We then map the lattice to a graph \mathcal{G} , and all information of \mathcal{G} is stored in the degree matrix \mathbf{D} and adjacent matrix \mathcal{A} , as shown in Fig.6.a. The convolution is performed by using the Laplacian matrix $\mathbf{L} = \mathbf{D} - \mathcal{A}$. The input features are specified by the feature matrix $\mathbf{X} = (s_1^T, \dots, s_N^T)^T \in \mathbb{R}^{N \times 3}$, where $s_i = (x_i, y_i, z_i)$ is the spin at site i . Next, we apply the random walk normalized Laplacian $\mathbf{L}^{rm} = \mathbf{D}^{-1}\mathbf{L}$ to aggregate the features, and use the ReLu function as an activation function to get the feature representation $\mathbf{H} \in \mathbb{R}^{N \times 1}$ (see Fig.6.b)

$$\mathbf{H} = \text{ReLu}(\mathbf{L}^{rm}\mathbf{X}\mathbf{W}_h + \mathbf{b}_h) \quad (6)$$

where $\mathbf{W}_h \in \mathbb{R}^{3 \times 1}$ and $\mathbf{b}_h \in \mathbb{R}^{N \times 1}$ are both learnable parameters. Finally, by using the fully connected layer and the *softmax* function to aggregate \mathbf{H} , we get the output feature (see Fig.6.c)

$$\hat{\mathbf{Y}} = \text{softmax}(\mathbf{H}^T\mathbf{W}_p + \mathbf{b}_p) \quad (7)$$

where $\mathbf{W}_p \in \mathbb{R}^{N \times 2}$ and $\mathbf{b}_p \in \mathbb{R}^2$ are also learnable parameters. The two components of the output feature $\hat{\mathbf{Y}} \in \mathbb{R}^2$ respectively correspond to the classification confidences of ordered phase (p_o) and disordered phase (p_d). It is reasonable to address $p_o = p_d$ at the critical temperature T_c .

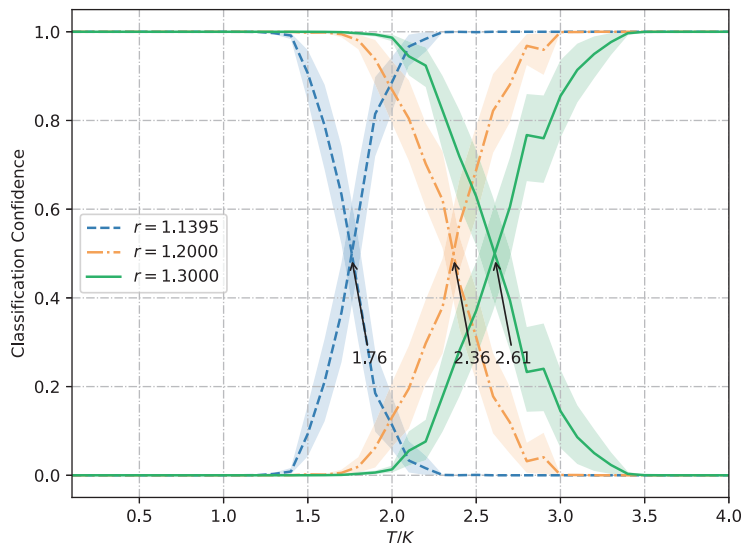


Figure 7: Critical temperature of spherical Fibonacci-lattice XY models, which is determined by the classification confidences: $p_o = p_d$. The blue dashed, brown dot-dashed and green solid curves correspond to $r_c = 1.1395, 1.2$ and 1.3 respectively.

In Figure.7, we plot classification confidences vs temperature for $r_c = 1.1395, 1.2$ and 1.3 . The critical temperature is determined by $p_o = p_d$. The translucent region of each curve indicates the 95% confidence interval. It can be found that T_c increases as r_c increases, which is quite understandable. Note a larger r_c means the interaction between different spins is stronger. Thus, one needs more energetic thermal fluctuations to break topological vortices, which means higher T_c . We also want to emphasize that due to the randomness of model training, there might exist a small error between different training results.

V. VORTEX DYNAMICS

It is interesting to find out how the vortices move on the sphere during a MC annealing. In fact, the number of MC attempts is related to the real time via a certain function $f: n = f(t)$ [48]. Hence the MC simulation, which brings a system to equilibrium from a nonequilibrium starting point, is equivalent to the spontaneous relaxation dynamics governed by the Langevin equation[48, 49]. Physically, the trajectory actually describes the time-dependent evolution of vortices on a sphere, and $n = f(t)$ can be thought of as a reparametrization of the evolutionary path. To trace the motion of vortices, we need to locate where a vortex is at first. Previous discussions have shown that the GCN has a superior performance on recognizing ordered/disordered phases of spherical XY models, even with only one convolutional layer. This has a qualitative explanation. For a one-convolutional-layer GCN, the Laplacian matrix realizes the feature aggregation of the neighbors for each site, i.e.

$$\mathbf{R} = \mathbf{L}^{\text{rm}} \mathbf{X} = (\mathbf{r}_1^T, \dots, \mathbf{r}_N^T)^T \quad (8)$$

where $\mathbf{r}_i = \frac{1}{\|\mathcal{E}_i\|} \sum_{j \in \mathcal{E}_i} (\mathbf{s}_j - \mathbf{s}_i)$, and \mathcal{E}_i is the set of neighbors of site i . This provides a good indicator to probe the local orderedness. At sites where there are no vortices, the spin changes slowly, thus $\|\mathbf{r}_i\|$ is close to zero. On the contrary, at sites where there exist vortices, the spin changes dramatically, and $\|\mathbf{r}_i\|$ must be finite. Hence, we define $\xi_i = \|\mathbf{r}_i\|$ as the local disorderedness at site i . To detect vortices, we set a threshold $\Delta = \gamma \|\bar{\mathbf{r}}\|$, where $\|\bar{\mathbf{r}}\| = \frac{1}{N} \sum_i \|\mathbf{r}_i\|$ is the average local disorderedness, and γ is an adjustable parameter. As a check of this method, we apply it to a 30×30 square-lattice XY model and present the result in Fig.8. Evidently, all vortices are precisely probed by their local disorderedness.

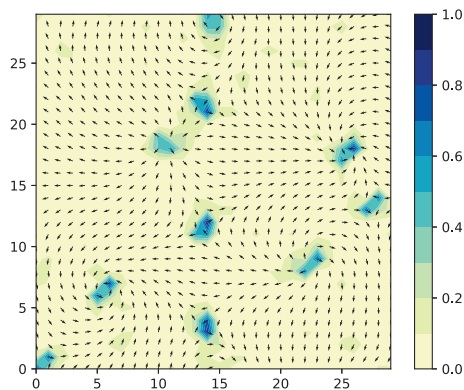


Figure 8: The local disorderedness of vortices in a 2D square-lattice XY model.

We then apply the method to the spherical XY model. After finding the vortices, we are going to trace their evolutionary paths as the MC simulation continues, which can be achieved by a data clustering algorithm. Specifically, we first filter out the coordinates such that $\xi_i > \Delta$ at every 10000 steps, which obviously belong to certain vortices. We label the set of these coordinates by P , and further use a well known machine learning method, the density-based spatial clustering of applications with noise (DBSCAN)[50], to group these coordinates by vortices:

$$\{P_1, \dots, P_k\} = \text{DBSCAN}(\text{Minpts}, r, P). \quad (9)$$

Here Minpts and r are two required parameters, K is the number of different vortices, and $P_i (i \in \{1, \dots, k\})$ is the classified coordinate-set, each of which belongs to a single vortex. The position of a vortex is given by

$$\mathbf{x}_i^v = \underset{\|\mathbf{x}\|=R}{\text{argmin}} \sum_{\mathbf{x}^p \in P_i} \|\mathbf{x} - \mathbf{x}^p\|^2. \quad (10)$$

With these tools, we finally obtain the dynamical picture of vortices on a spherical surface. We visualize our results with $N = 1000$, $r_c = 1.1395$ and $T = 0.001K$ in Fig.9. Previous results have shown that initially there are multiple vortices and finally only two of them survive. In the upper row, we present the merging process of a pair of vortices with different topological charges. The first two subgraphs show the initial and intermediate positions of these vortices,

and the last one gives the their merging path. In the lower row, we present the distance between two vortices which finally survive as a function of the MC step. The whole figure tells that during the MC annealing, some vortices disappear or merge with each other, and the remaining two tend to keep apart due to the repulsion between them since their carry same charges.

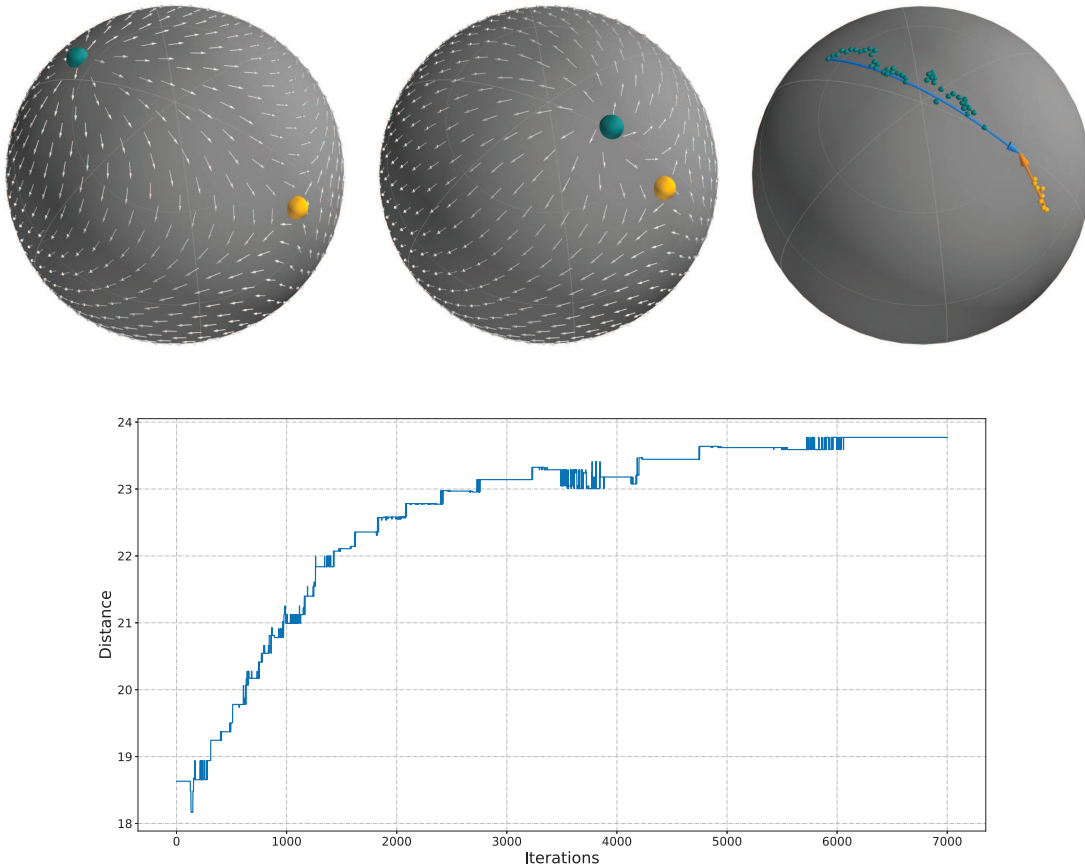


Figure 9: (Upper panels) Evolutionary trajectories of two vortices. (Lower panel) Distance between two vortices as a function of Monte Carlo steps.

VI. CONCLUSION

In this paper, we study the interesting features of XY models confined on the surface of a sphere. This is triggered by the planned experiments on cold atomic gases in microgravity environments such as the International Space Station. We consider the Fibonacci lattice, an almost uniform spherical lattice, and use MC simulations and new powerful machine learning techniques, such as the GCN model, to predict the vortex distributions and phase transition temperatures. By performing the DBSCAN clustering, we also draw the evolutionary path of vortices on the sphere during a MC annealing. Our results may shed some light on the future space-based experiments on spherically confined atomic gases.

H. G. was supported by the National Natural Science Foundation of China (Grant No. 12074064). We also thank Prof. Chih-Chun Chien for profitable discussions and suggestions.

Appendix A: Introduction to GCN

1. Problem Formulation

Our aim is to distinguish the ordered phase at low temperatures and disordered phase at high temperatures of the spherical XY model by using GCN. Specifically, we are going to obtain a classification function $\hat{\mathbf{Y}} = F(\mathbf{X}, \Theta)$ by data training, which maps the feature matrix \mathbf{X} containing all spin information into the label space $\hat{\mathbf{Y}} = (p_o, p_d)$. Here p_o and p_d respectively give the classification confidences of the ordered and disordered phases. The training process is to adjust the set Θ of parameters such that the classification result $\hat{\mathbf{Y}}$ is as close to the real label \mathbf{Y} as possible.

2. Preliminaries

Graph is a powerful data structure for processing relational information, which can effectively realize the clustering of neighbor information. A graph \mathcal{G} comprises a set \mathcal{V} of vertices and a set \mathcal{E} of edges. For two vertices $v_i, v_j \in \mathcal{V}$, if there exists an edge $e_{ij} \in \mathcal{E}$, v_i and v_j are said to be connected by e_{ij} in the graph drawing in \mathcal{G} . The number of vertices to which a vertex v_i is linked is defined as the degree d_j of v_i . Explicitly, \mathcal{G} can be represented by the adjacent matrix \mathcal{A} , of which the entries are given by $\mathcal{A}_{ij} = 1$ if $e_{ij} \in \mathcal{E}$, or 0 otherwise. The feature of each vertex v_i can be expressed by a d -dimensional vector \mathbf{x}_i . Thus, for all vertices, their features can be represented by a matrix $\mathbf{X} \in \mathbb{R}^{n \times d}$, where n is the degree of \mathcal{G} .

GCN is a generalization of the traditional CNN, which can be used to classify vertices and graphs. There are many ways to realize GCN, which may be mainly classified into spatial-based and spectral-based convolutions. Both of them can be realized with the help of the Laplacian matrix L , defined by $L = D - \mathcal{A}$, where \mathcal{A} is aforementioned adjacent matrix, and D is a diagonal matrix called degree matrix, of which the diagonal elements are the degrees of vertices. The definition of Laplacian matrix is not unique, and the frequently-used definitions include the symmetric normalized Laplacian $L^{\text{sym}} = D^{-\frac{1}{2}}LD^{-\frac{1}{2}}$ and the random walk normalized Laplacian $L^{\text{rw}} = D^{-1}L$.

The spatial-based GCN can be expressed by

$$\mathbf{H}^{l+1} = \sigma(\mathbf{L}\mathbf{H}^l\mathbf{W}^l) \quad (\text{A1})$$

where \mathbf{W} is the set of learnable parameters, \mathbf{H}^l is the feature of the l -th layer (Note \mathbf{H}^0 represents the input feature), and $\sigma(\cdot)$ is the activation function. In this method, the feature of each vertex is obtained by aggregating the information of its neighbours.

The spectral-based GCN is realized by taking the spectral decomposition of the Laplacian matrix (i.e. the Fourier transformation) firstly and performing the associated inverse transformation secondly. It can be expressed by

$$\mathbf{H}^{l+1} = \sigma(\mathbf{U}g_\theta(\mathbf{\Lambda})\mathbf{U}^T\mathbf{H}^l) \quad (\text{A2})$$

where \mathbf{U} is the matrix comprised by the eigenvectors of L , $\mathbf{\Lambda}$ is the diagonal matrix comprised by the eigenvalues of L , and the convolutional kernel $g_\theta(\mathbf{\Lambda})$ represents the set of learnable parameters. A widely-adopted choice of g_θ is the Chebyshev polynomial, which can reduce the number of steps of eigendecomposition and is thus more suitable for large-scale graph networks.

3. Methodology of Phase Classification

Here we illustrate how to apply GCN to recognize different phases of the spherical XY model, which is shown schematically by flow charts in Fig.6. The convolutional kernel of traditional CNNs can capture the local spatial information, which corresponds to the short-range orderedness of square XY models at low temperatures. This is why traditional CNN works well in these situations. Note the key point in phase-recognition is to effectively aggregate the local spatial information. For XY models, the first step toward this is to establish the neighbour relation of each spin, which is guaranteed by the homogeneity of the square lattice. However, no such lattices exist on a spherical surface, and the Fibonacci lattice is only an approximate uniform lattice which has no translation invariance. Thus, the traditional CNN does not apply here. Fortunately, GCN instead provide an ideal structure to characterize the neighbour relation of irregular lattices. For a spherical Fibonacci lattice, all sites naturally comprise a set of vertices \mathcal{V} . Moreover, by choosing a critical radius r_c such that $e_{ij} \in \mathcal{E}$ if $\|\mathbf{r}_i - \mathbf{r}_j\| < r_c$, a graph \mathcal{G} can be constructed. To better capture local features, the value of r_c must be carefully selected such that each site is only linked to nearby sites. For example, when $N = 1000$, $R = 10$, the (almost) best choice is $r_c = 1.1395$, shown in Fig.6.a. In such a

spherical XY model, the spin at site i is denoted by a unit vector $\mathbf{s}_i = (x_i, y_i, z_i)$ with $i = 1, 2, \dots, N$. Thus, the feature matrix is given by $\mathbf{X} = (\mathbf{s}_1^T, \dots, \mathbf{s}_N^T)^T \in \mathbb{R}^{N \times 3}$. In this paper, we use the random walk normalized Laplacian $\mathbf{L}^{rm} = \mathbf{D}^{-1}\mathbf{L}$ to aggregate the features, and apply the ReLu function as the activation function, as shown in Fig.6.b

$$\mathbf{H} = \text{ReLu}(\mathbf{L}^{rm}\mathbf{X}\mathbf{W}_h + \mathbf{b}_h) \quad (\text{A3})$$

where $\mathbf{W}_h \in \mathbb{R}^{3 \times 1}$ and $\mathbf{b}_h \in \mathbb{R}^{N \times 1}$ are both learnable parameters and $\mathbf{H} \in \mathbb{R}^{N \times 1}$ is the feature representation. We further use the full connected layer and the *softmax* function to aggregate the representation \mathbf{H} , as demonstrated in Fig.6.c, which can also be expressed by

$$\hat{\mathbf{Y}} = \text{softmax}(\mathbf{H}^T\mathbf{W}_p + \mathbf{b}_p) \quad (\text{A4})$$

where $\mathbf{W}_p \in \mathbb{R}^{N \times 2}$ and $\mathbf{b}_p \in \mathbb{R}^2$ are both learnable parameters, and the output $\hat{\mathbf{Y}} \in \mathbb{R}^2$ give the classification confidences that the input features respectively correspond to ordered/disordered phases.

4. Experiment Design

1. *General settings*: The trial data comes from MC simulations. As an example, we generate a $N = 1000$ Fibonacci lattice on a spherical surface of radius $R = 10$. On the tangent plain of each lattice site, a randomly-oriented spin is assigned initially. When mapping the lattice into a graph, we choose $r_c = 1.1395$ and use the cross entropy function as the loss function.

2. *Data settings*: At first, we give a very rough estimation of the critical temperature T_c by several runs of MC simulation, which shows $T_c \sim 2\text{K}$. Then, at temperatures far below T_c , we perform MC simulations over the temperature range $[0.01, 0.5]\text{K}$ with a spacing of 0.01K , and get a data set for spin distributions in low-temperature ordered phases. We repeat the simulation over the same temperature range for 12 times and get 12 sampling sets. Similarly, at temperature far above T_c , we perform MC simulations over the temperature range $[11, 60]\text{K}$ with a spacing of 1K , and get a data set for spin distributions in high-temperature disordered phases. We also repeat the simulations to get 12 sampling sets. Finally, we split them into the training sets, validation sets and test sets, which respectively have 10, 1 and 1 sampling set for ordered and disordered phases.

3. *Critical temperature*: The critical temperature can be precisely determined if our GCN model is trained sufficiently. We sample data in a temperature range in which T_c is included, and input these features into the GCN model. The output gives the confidences that the input features correspond to the ordered (p_o) and disordered phases (p_d). Obviously, $p_o + p_d = 1$. The critical temperature is specified if $p_o = p_d$. In order to diminish the errors, we carry out multiple simulations and classifications with the same set of parameters, and average the corresponding classification confidences. For example, we execute our algorithm in the range $[0.1, 4.0]\text{K}$ with a spacing of 0.05K , and repeat the procedure 50 times to average the confidences for $r_c = 1.1395, 1.20$ and 1.30 .

4. *Numerical Results*: When testing the GCN model with samples in test sets, it gives correct classification results of $\geq 99.9\%$ classification confidences and 100% accuracies, even with only one convolutional layer. We outline the numerical results in Figure.7.

-
- [1] E. Lieb, T. Schultz, and D. Mattis, Ann. Phys. **16**, 407 (1961).
 - [2] B. D, Physica **86-88B**, 556 (1977).
 - [3] J. M. Kosterlitz and D. J. Thouless, J. Phys. C **6**, 1181 (1973).
 - [4] J. M. Kosterlitz, J. Phys. C **7**, 1046 (1974).
 - [5] J. M. Kosterlitz, Rep. Prog. Phys. **79**, 026001 (2016).
 - [6] S. Katsura, T. Horiguchi, and M. Suzuki, Physica **46**, 67 (1970).
 - [7] L. J. de Jongh and A. R. Miedema, Adv. Phys. **23**, 1 (1974).
 - [8] J. Tobochnik and G. V. Chester, Phys. Rev. B **20**, 3761 (1979).
 - [9] R. Gupta and C. F. Baillie, Phys. Rev. B **45**, 2883 (1992).
 - [10] P. Olsson, Phys. Rev. B **46**, 14598 (1992).
 - [11] P. Olsson, Phys. Rev. B **52**, 4511 (1995).
 - [12] P. Olsson, Phys. Rev. B **52**, 4526 (1995).
 - [13] N. Nagaosa, *Quantum Field Theory in Condensed Matter Physics* (Springer and Beijing World Publishing Cooperation, Beijing, 2010).
 - [14] A. Altland and B. Simons, *Condensed Matter Field Theory* (Cambridge University Press and Beijing World Publishing Cooperation, Beijing, 2015).

- [15] X. G. Wen, *Quantum field theory of many-body systems* (Oxford University Press, Oxford, 2004).
- [16] L. Delfini, S. Lepri, and R. Liv, *J. Stat. Mech.-Theory Exp.* **2005**, P05006 (2005).
- [17] A. Kushima, X. Lin, J. Li, J. Eapen, J. C. Mauro, X. F. Qian, P. Diep, and S. Yip, *J. Chem. Phys.* **130**, 224504 (2009).
- [18] W. Zhang, J. Liu, and T.-C. Wei, *Phys. Rev. E* **99**, 032142 (2019).
- [19] J. Wang, W. Zhang, T. Hua, and T.-C. Wei, *Phys. Rev. Res.* **3**, 013704 (2021).
- [20] J. Struck, M. Weinberg, C. Ölschläger, P. Windpassinger, J. Simonet, K. Sengstock, R. Höppner, P. Hauke, A. Eckardt, L. M, et al., *Nat. Phys.* **9**, 738 (2013).
- [21] N. S. Móller, F. E. A. dos Santos, V. S. Bagnato, and A. Pelster, *New J. Phys.* **22**, 063059 (2020).
- [22] A. Tononi and L. Salasnich, *Phys. Rev. Lett.* **123**, 160403 (2019).
- [23] N. Lundblad, R. A. Carollo, C. Lannert, M. J. Gold, X. Jiang, D. Paseltiner, N. Sergay, and D. C. Aveline, *npj Microgravity* **5**, 30 (2019).
- [24] S. J. Bereta, M. A. Caracanhas, and A. L. Fetter, *Phys. Rev. A* **103**, 053306 (2021).
- [25] T. van Zoest and *et al.*, *Science* **328**, 1540 (2010).
- [26] N. Becker and *et al.*, *Nature* **562**, 391 (2018).
- [27] L. Wang, *Phys. Rev. B* **94**, 195105 (2016).
- [28] G. Carleo and M. Troyer, *Science* **355**, 602 (2017).
- [29] J. Carrasquilla and R. Melko, *Nat. Phys.* **13**, 431 (2017).
- [30] K. Ch'ng, J. Carrasquilla, R. Melko, and E. Khatami, *Phys. Rev. X* **7**, 031038 (2017).
- [31] D. Deng, X. Li, and S. Sarma, *Phys. Rev. X* **7**, 021021 (2017).
- [32] C. Wang and H. Zhai, *Phys. Rev. B* **96**, 144432 (2017).
- [33] D. Deng, X. Li, and S. Sarma, *Phys. Rev. B* **96**, 195145 (2017).
- [34] F. Schindler, N. Regnault, and T. Neupert, *Phys. Rev. B* **95**, 245134 (2017).
- [35] J. S. Wetzel, *Phys. Rev. E* **96**, 022140 (2017).
- [36] W. Hu, R. Singh, and R. Scalettar, *Phys. Rev. E* **95**, 062122 (2017).
- [37] K. Ch'ng, N. Vazquez, and E. Khatami, *Phys. Rev. E* **97**, 013306 (2018).
- [38] P. Zhang, H. Shen, and H. Zhai, *Phys. Rev. Lett.* **120**, 066401 (2018).
- [39] J. Venderley, V. Khemani, and E. Kim, *Phys. Rev. Lett.* **120**, 257204 (2018).
- [40] R. Dixon, *Mathographics* (Dover Publications, New York, 1997).
- [41] Á. González, *Math. Geosci.* **42**, 49–64 (2010).
- [42] J. W. Milnor, *Topology from the Differentiable Viewpoint* (Princeton University Press, Princeton, 1997).
- [43] R. L. B. Selinger, A. Konya, A. Travesset, and J. V. Selinger, *J. Phys. Chem. B* **115**, 13989 (2011).
- [44] M. Beach, A. Golubeva, and R. Melko, *Phys. Rev. B* **97**, 045207 (2018).
- [45] W. Zhang, J. Liu, and T.-C. Wei, *Phys. Rev. E* **99**, 032142 (2019).
- [46] J. Zhou, G. Cui, S. Hu, Z. Zhang, C. Yang, Z. Liu, L. Wang, C. Li, and M. Sun, *AI Open* **1**, 57 (2020).
- [47] Z. Zhang, P. Cui, and W. Zhu, *IEEE Transactions on Knowledge and Data Engineering* pp. 1–1 (2020).
- [48] P. Meakin, H. Metiu, R. G. Petschek, and D. J. Scalapino, *J. Chem. Phys.* **79**, 1948 (1983).
- [49] R. Loft and T. A. Deorand, *Phys. Rev. B* **35**, 8528 (1987).
- [50] M. Ester, H.-P. Kriegel, J. Sander, and X. Xu, in *KDD-96 Proc.* (Menlo Park, CA, USA, 1996), pp. 226–231.